Applied Computing and Geosciences 24 (2024) 100207

Contents lists available at ScienceDirect

Applied Computing and Geosciences

journal homepage: www.sciencedirect.com/journal/applied-computing-and-geosciences

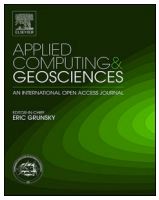

A machine learning approach for mapping susceptibility to land subsidence caused by ground water extraction

Diana Orlandi [a,*], Esteban Díaz [b], Roberto Tomás [b], Federico A. Galatolo [a], Mario G.C.A. Cimino [a], Carolina Pagli [c], Nicola Perilli [d]

[a] Dept. of Information Engineering, University of Pisa, Pisa, 56122, Italy
[b] Dept. of Civil Engineering, University of Alicante, Alicante, 03080, Spain
[c] Dept. of Earth Sciences, University of Pisa, Pisa, 56126, Italy
[d] Dept. of Civil and Industrial Engineering, University of Pisa, Pisa, 56122, Italy

ARTICLE INFO

Keywords:
Land subsidence
Susceptibility mapping
Machine learning
InSAR

ABSTRACT

Land subsidence is a worldwide threat that may cause irreversible damage to the environment and the infrastructures. Thus, identifying and mapping areas prone to land subsidence with accurate methods such as Land Subsidence Susceptibility Index (LSSI) mapping is crucial for mitigating the adverse impacts of this geohazard. Also, Machine Learning (ML) is now becoming a powerful tool to analyze vast and different datasets such as those necessary for LSSI mapping. In this study, we use the conventional Frequency Ratio (FR) method and ML models to generate LSSI maps of the region of Murcia (Spain) where land subsidence occurred in the past due to groundwater overdraft. A LSSI map was initially generated with known FR. Then, additional Conditioning Factors (CFs) with increased spatial resolution were used to train several ML models and generate a new LSSI map. The Extra-Trees Classifier (ETC) outperformed the other approaches, achieving the best performance with a weighted average precision and F1-Score of 0.96, after optimizing its hyperparameters. Then, a third LSSI map was calculated using the FR method and observations of land subsidence from InSAR (Interferometric Synthetic Aperture Radar). This study shows that the effectiveness of using several CFs depends on the added information of each layer. Moreover, the comparison between the different LSSI maps and InSAR data highlights the crucial role of the spatial resolution for accurate mapping, thus enhancing land subsidence risk assessment.

1. Introduction

Land subsidence refers to the lowering of the ground surface caused by natural or anthropogenic processes such as groundwater withdrawal. It is a worldwide threat that affects several areas in the world (Galloway and Burbey, 2011). Well-known examples can be found in the Po Valley, northern Italy (Fabris et al., 2022), Guadalentín basin in Spain (Hu et al., 2022) and metropolitan areas such as Mexico City (Cigna and Tapete, 2021) and Murcia (Tomás et al., 2005) where structures built in subsiding areas suffer damage and collapse (Tomás et al., 2005). Thus, identifying and mapping areas prone to land subsidence is important for planners and decision-makers to ensure adequate management of the territory and to minimize the associated impacts (Herrera et al., 2020).

In the literature, a wide range of techniques have been employed, both qualitative and quantitative, to assess and map Land Subsidence Susceptibility (LSS) in different contexts, such as in areas of sinkholes, earthquake damage, and over-exploited aquifer. The susceptibility to land subsidence of a region is usually evaluated by using maps of susceptibility indexes that vary spatially. These maps are usually generated by integrating different layers of information related to Conditioning Factors (CFs) such as geological or geotechnical units, land use, soil thickness, and aquifer units. Each CF is characterized by multiple classes that can be represented on a map. The availability of a vast range of potential CFs and classes is essential for generating accurate LSS maps. The overall purpose is to generate a model based on expert knowledge or on known values of land subsidence that link CFs and LSS. These maps can be difficult to obtain because the relationships between CFs and land subsidence are diverse, acting at different scales and times, and because direct and regular land subsidence measurements are often lacking (Herrera et al., 2020).

A conventional semi-quantitative method for mapping LSS is the Weighted Linear Combination (WLC), where each CF is weighted, and

* Corresponding author. Dept. of Information Engineering, University of Pisa, via G. Caruso 16, Pisa, 56122, Italy.
E-mail address: diana.orlandi@phd.unipi.it (D. Orlandi).

https://doi.org/10.1016/j.acags.2024.100207
Received 3 May 2024; Received in revised form 11 November 2024; Accepted 14 November 2024
Available online 16 November 2024

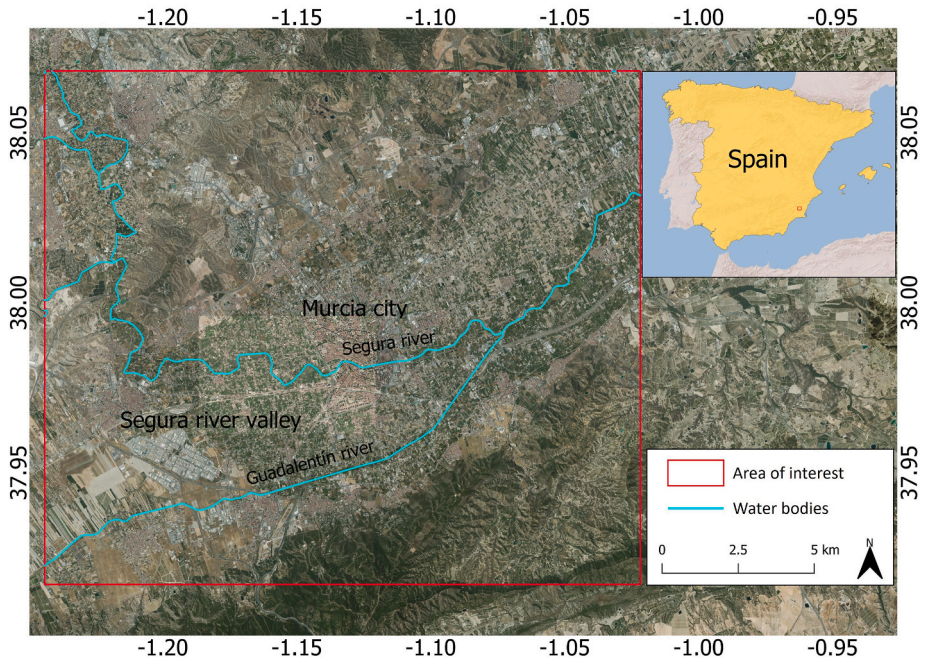

Fig. 1. Map of the area of interest (AOI).

all its classes are rated based on expert knowledge and historical inventories (Loupasakis and Tzampoglou, 2017). Other methods include Analytical Hierarchy Process (AHP), which used expert judgment to weight and rank factors and Certain Factor (CtF) analysis, which quantifies the influence of various factors on LSS based on their correlation and importance (Rezaei et al., 2020). However, a major limitation of these methods is their dependence on expert knowledge, which often introduces uncertainties tied to the subjective opinions of decision makers (Pradhan et al., 2014).

On the other hand, approaches such as Fuzzy Logic (FL) (Bianchini et al., 2019) and Frequency Ratio (FR) (Herrera et al., 2020; Bianchini et al., 2019; Elmahdy et al., 2020) can also be used. In particular, FL uses membership functions to handle uncertainty and classifies susceptibility based on input factors and their nonlinear relationships. The FR method defines the correlation between the land subsidence and the related factors in a given spatial domain. The FR is then the ratio of occurrence to non-occurrence probability for a specific phenomenon (Bianchini et al., 2019). Bianchini et al. (2019) used multi-temporal InSAR (Interferometric Synthetic Aperture Radar) data as a Spatial Database (SD) and mapped the land subsidence susceptibility in the area of Grosseto Plain (Italy) by testing both FL and FR approaches. From their analysis it emerged that the performance of FR was better than FL. Another work was published by Herrera et al. (2020), where FR was used to evaluate and map LSS at a global scale using the Land Subsidence Susceptibility Index (LSSI). In particular, the authors created a Global Subsidence Database (GSDB) consisting of a set of known land subsidence locations and several CFs. They then used FR to extrapolate CF weights that were then used to map LSSI globally and thus obtain a Global Subsidence Susceptibility (GSS) map.

Moreover, the FR method has also been tested and combined with Machine Learning (ML) algorithms such as Random Forest (RF), which employs an ensemble of decision trees to classify susceptibility, improving model accuracy and robustness (Elmahdy et al., 2020). In fact, in the last decade, Artificial Intelligence (AI) and ML techniques have been demonstrated to be powerful tools to overcome the limitations of semi-quantitative methods, such as those involving imbalanced datasets and multi-classification tasks. Several machine learning models have been created for predicting geo-environmental hazards spatially. These include 1) Decision Tree (DT), which uses a branching structure to classify susceptibility based on input features (Arabameri et al., 2021), 2) Logistic Model Tree (LMT) that combines decision trees with logistic regression (Tien Bui et al., 2018), 3) Support Vector Machine (SVM) that finds optimal hyperplanes to classify data (Arabameri et al., 2021; Tien Bui et al., 2018), and 4) Maximum Entropy (MaxEnt) which estimates the probability distribution of data for classification (Rahmati et al., 2019).

In this context, a significant line of work was developed in (Saha et al., 2023) to build the relationship between climate change and land subsidence using Deep Learning models. In particular, the authors discussed the relationship between deformation and ground-water level change, as well as extreme precipitation. Further, the authors used a Deep Learning model to establish the link between groundwater level and satellite observations of ground deformation, and then obtained the link between the drivers of the dualistic water cycle and land subsidence.

In the context of hybrid models for Land Susceptibility Maps, relevant research work was developed in (Wang et al., 2024) from both conventional and ML models, combining AHP and SVM models. A limitation of this research is the lack of deep learning methods by increasing datasets.

In our work, the land subsidence of the Vega Media del Segura River (Murcia, SE Spain) induced by groundwater withdrawal was evaluated by means of LSSI mapping as defined by Herrera et al. (2020). We therefore use the Frequency Ratio (FR) and Machine Learning (ML) methods. A significant advancement of this study is the use of an expanded set of CFs with higher spatial resolution, offering a more detailed representation of the LSSI of the area. Moreover, the generated LSSI maps were compared to the land subsidence measured by InSAR.

The paper is structured as follows. The study area and the dataset used are described in Section 2 and Section 3, respectively, whereas the methodologies adopted to generate the different LSSI maps are detailed in Section 4. The results and the discussion are in section 5. Conclusions are covered by Section 6.

2. Study area

The study area focuses on the Vega Media of the Segura River Basin, situated in southeastern Spain. It covers approximately 326 km^2,

Table 1
List of CFs collected over the AOI.

CFs available in GSS (Herrera et al., 2020)		CFs prepared for this study						
CFs	Spatial resolution (m)	CFs	Spatial resolution (m)	# Classes	Categorical/ Numerical	Short description	Vector/ Raster	Source
Geological units	1000 × 1000	Geotechnical units	–	5	Categorical	Geotechnical units	Vector	(European Environment Agency (EEA), 2006)
Land cover	1000 × 1000	Land cover	–	19	Categorical	Land cover classification	Vector	(Organismo Autónomo Centro Nacional de Información Geográfica (CNIG), 2023)
Slope	1000 × 1000	Slope	20 × 30		Numerical	Rate of change of elevation (°)	Raster	Derived from digital elevation model (Beck et al., 2018; Bagheri-Gavkosh et al., 2021)
Climate	9000 × 9000	Climate	1000 × 1000	3	Categorical	Climate classification	Raster	(Bagheri-Gavkosh et al., 2021; IGME, 2000)
–	–	Elevation	20 × 30		Numerical	Topography	Raster	(Beck et al., 2018; Bagheri-Gavkosh et al., 2021)
–	–	Soft soil thickness	–	7	Numerical	Thickness of first soil strata	Vector	(IGME, 2000; Confederación Hidrográfica del Segura, 2023)
–	–	River distance	20 × 30		Numerical	Buffer map of distance from river	Vector	Derived from river vector map (Confederación Hidrográfica del Segura, 2023; Pedregosa et al., 2011)

including the metropolitan area of Murcia intersected by the Segura and Guadalentín rivers (Fig. 1). The Vega Media of the Segura River is an alluvial plain characterized by its flat topography and fertile soils, which have been shaped by fluvial processes. Floodplains are the primary landforms, formed by the deposition of sediments during periodic flooding events. The geological framework of the Vega Media of the Segura River is complex, influenced by tectonic activities and sedimentary processes acting over millions of years. The study area is located in the eastern sector of the Betic Cordillera (Herrera et al., 2010), a mountain range formed by the collision of the African and Eurasian plates. Since the Upper Miocene, the zone has experienced compressional tectonics that led to the development of the foreland basin of the Vega Media of the Segura. The basin is delimited by Permo-Triassic rocks from the basement belonging to the internal zones of the Betic Cordillera in the south and Neogene sedimentary rocks in the north (Tessitore et al., 2016). It is filled by Plio-Quaternary sediments of the Segura River divided in three main units: the upper Miocene marls (the lowest unit), a clastic succession of marls and clays of Pliocene-Quaternary age (the intermediate unit) and Recent sediments (the uppermost unit) deposited by the Segura and Guadalentín rivers (Tomás et al., 2005). These Recent sediments constitute the most problematic geotechnical unit. Within a hydraulic framework, the aquifer system is composed of two main units: a shallow semi-confined aquifer made of fine soils which reach 30 m below the surface (Herrera et al., 2010), below which is a deep aquifer made of sand and gravels from which groundwater has been extensively pumped in the past (Tomás et al., 2005; Tomas et al., 2011). In particular, the Vega Media of the Segura was widely affected by land subsidence in the nineties reaching maximum values of up to 15 cm (Tomas et al., 2011). The land subsidence intensified during drought periods leading to lowering piezometric levels. The first documented episode of land subsidence was caused by a lowering of the piezometric level of 8 m and occurred during a period of drought in 1992–1995. InSAR measurements show reduced land subsidence rates between 1993 and 1995 mainly in the southwestern part of Murcia. However, in 1995–1997, land subsidence increased especially in the southwest and northeast portions of the city, showing deformation velocities of up to 10 mm/yr (Tomás et al., 2005). Lastly, during the period of 1998–2004, vertical displacements of 2 mm/yr were observed in the central part of the basin filled by Recent and unconsolidated sediments (Tomás et al., 2005). Although the area affected by land subsidence extends beyond the limits of the Vega Media in the Segura Basin, our analysis specifically focused on the administrative area of the basin, including the city of Murcia, where the highest subsidence rates were recorded. During the first drought episode, over 150 buildings and other infrastructure in this area were damaged (Tomás et al., 2005). This selection of the study area was also driven by the fact that some of the CFs used in the analysis, such as "soft soil thickness" were collected exclusively within the administrative area of the Vega Media of the Segura River Basin.

3. Data

In this work, a fundamental starting point was the global map of LSS developed by Herrera et al. (2020). In their work, the authors used the FR method (explained in detail in section 3.3) to calculate the different weights of the classes in each CF (geological units, land cover, slope and climate) based on the analysis of real ground deformation from 200 different locations in the world, and to obtain a global LSSI map, namely a GSS map. As established by the authors, the GSS map is classified globally into six LSSI levels, each representing an increasing severity of land subsidence susceptibility. Level 1 is "Very Low" and represents areas with minimal susceptibility of subsidence, typically found in regions with stable geotechnical units, high elevation, and steep slopes, where infrastructure is unlikely to be affected by land subsidence. Level 2 is "Low" and represents areas with slight susceptibility, where minor factors, such as low slope and low soft soil thickness, may contribute to ground instability, causing little to no damage. Level 3 is "Medium Low", which might present moderate susceptibility, where soft soil layers are present and land subsidence can occur, but it is not expected to be widespread or severe. In Level 4, which is "Medium High", a noticeable susceptibility of subsidence is expected, as the area may include factors like low elevation and proximity to rivers, making it prone to ground deformation. Finally, Level 5 and 6, which are "High" and "Very High" classes, refer to areas with significant or extreme susceptibility of land subsidence, commonly characterized by thick soft soil layers, fine-grained geotechnical units and dry climate conditions (Cimino et al., 2022). These zones require extensive monitoring and strong preventive measures to mitigate their high susceptibility to land subsidence. However, this map is obtained at the spatial resolution of 1 km, leading to less detailed layers. In contrast, our study employed a higher number of CFs collected at a higher resolution, representing more local data. Table 1 presents a detailed overview of the characteristics of each CF used in this study compared to the dataset used by Herrera et al. (2020).

In our study, a total of seven thematic layers of CFs associated with the land subsidence of Murcia have been collected (Table 1). Fig. 2a–g shows the different classes for each of the thematic layers of the CFs, represented in different colors. It can be observed that the first four CFs

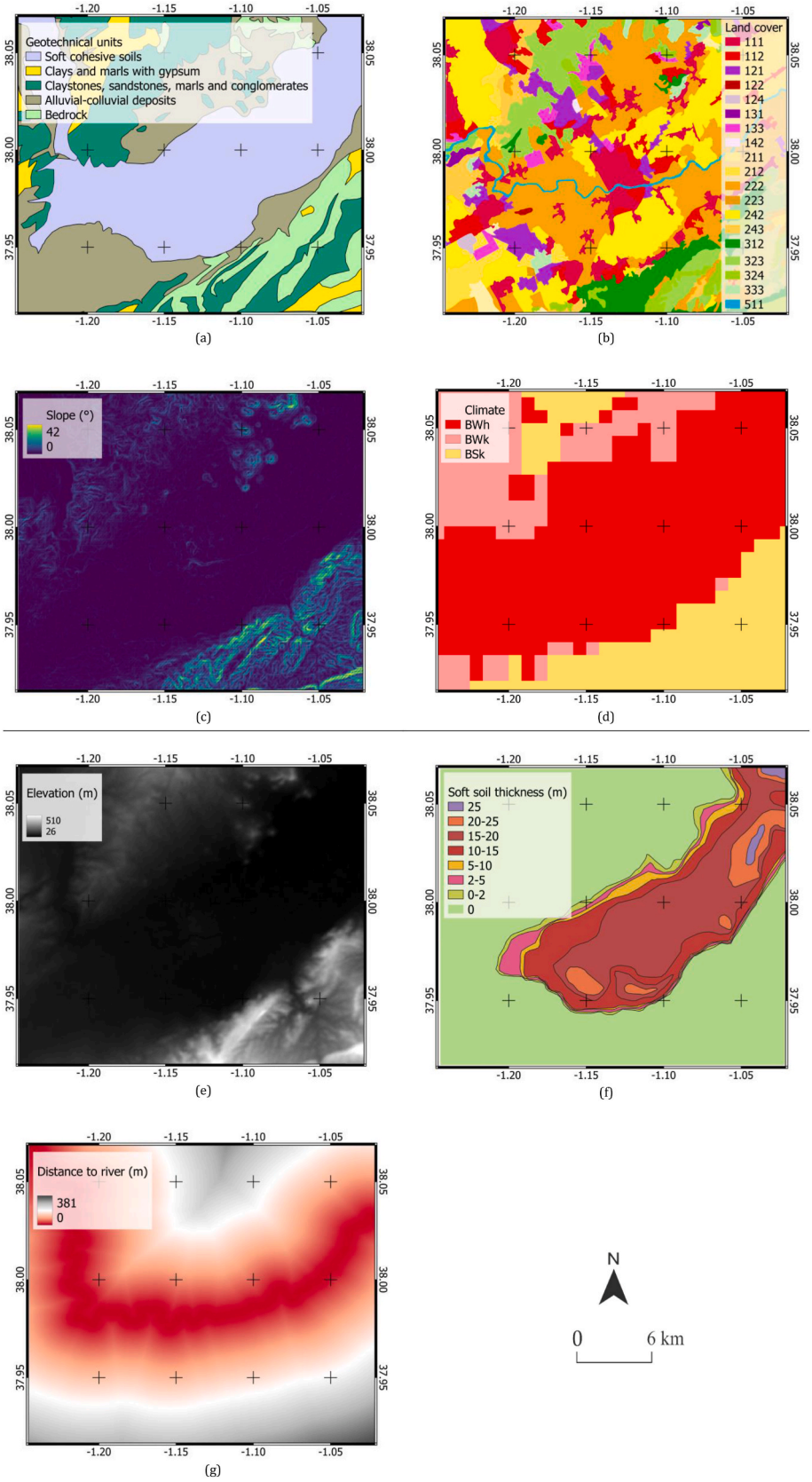

Fig. 2. Thematic maps depicting each CF within the AOI: a) geotechnical units; b) land cover (for a description of the classes see table S1); c) soft soil thickness; d) climate (for a description of the classes see table S1); e) elevation; f) slope; g) river distance. The definition of the classes plotted in figures b and d is included in the supplementary material. For a detailed overview of the characteristics and sources of each CF see Table 1.

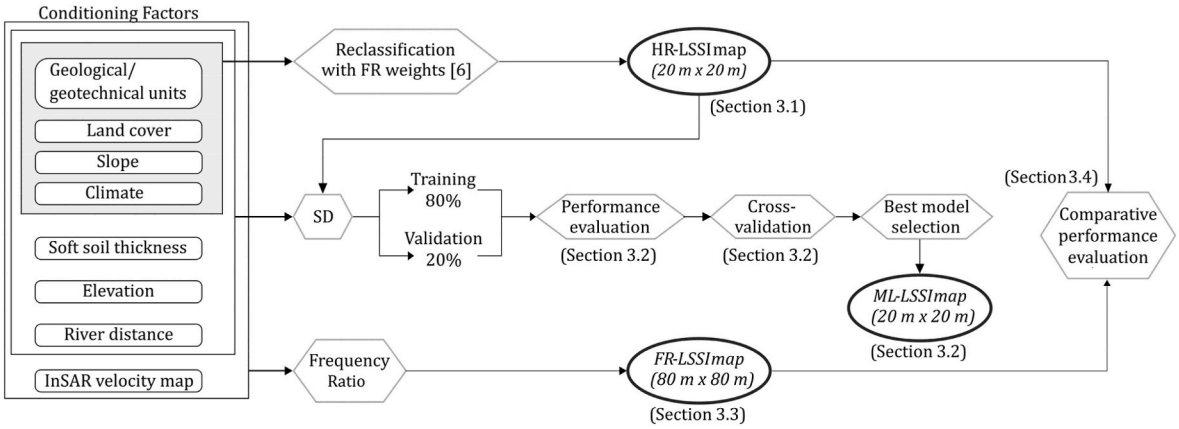

Fig. 3. Overall workflow for generating and validating the LSSI maps.

we used are similar to Herrera et al. (2020), except for "geological units" being replaced by "geotechnical units" and also including "land cover", "slope" and "climate". The "geotechnical units" (Comunidad Autónoma de la Región de Murcia, 2023) represents different soil and rock types categorized by their mechanical properties, indicating areas with varying ground stability and subsidence susceptibility. Moreover, the "land cover" layer shows the distribution of different surface types over the study area retrieved by the 2006 Copernicus CORINE land cover data (European Environment Agency (EEA), 2006). On the other hand, "slope" layer (Organismo Autónomo Centro Nacional de Información Geográfica (CNIG), 2023) was derived from the "elevation" layer using GIS tools, capturing steepness variations that might influence ground stability: typically, areas with low slope values are more prone to accumulation of water and fine sediments, making them more susceptible to land subsidence and to climate conditions that can affect soil moisture and groundwater dynamics. Notably, climate can play a crucial role as a CF in land subsidence susceptibility due to its impact on various environmental and geological processes. Specifically, Herrera-Garcia et al. (Herrera et al., 2020) emphasized the role of climate change in exacerbating subsidence risks through altered precipitation patterns and increased frequency of extreme weather events. Accordingly, in the area of Murcia, BWh class (hot, arid deserts) is a dominant climate type, correlated with higher susceptibility to land subsidence, especially in an urban setting. In addition, Bagheri-Gavkosh et al. (2021) discovered that climate factors, such as precipitation and temperature, significantly influence land subsidence rates. Based on Köppen's climate classification (Beck et al., 2018), they found that the highest LS rates occur in dry regions, while the lowest rates are observed in warm temperate areas. Furthermore, they noted that droughts in arid and semi-arid climates intensify groundwater depletion, which accelerates subsidence. Additionally, their research showed a negative correlation between LS and the aridity index, indicating that LS decreases as the aridity index increases. Consequently, a hot desert climate is particularly associated with higher LS rates due to more severe groundwater depletion and soil desiccation, making these areas more susceptible to subsidence. Additionally, in our study we include three additional factors including "elevation", "soft soil thickness" and "river distance". The layer of "elevation" (Organismo Autónomo Centro Nacional de Información Geográfica (CNIG), 2023), representing the height of the terrain above sea level, influencing factors such as water flow, erosion and soil stability. Thus, similarly to the "slope", it affects land subsidence susceptibility and geotechnical conditions because lower elevation areas often have higher groundwater accumulation and softer sediments, making them more prone to land subsidence. Notably, the layer of "soft soil thickness", which refers to the depth of weak, compressible soils, is extracted by the data collected specifically over the city of Murcia, where most of the damage and effects of land subsidence were found (Tomás et al., 2005; IGME, 2000). Furthermore, the layer of "river distance" (Confederación Hidrográfica del Segura, 2023) was calculated in a GIS environment to see the influence of the Segura and Guadalentín rivers on the LSS phenomenon. For all the above-mentioned CF layers the spatial resolution has been improved at a finer local scale. The minimum spatial resolution in the previous study was of 1 km, whereas it is 20 m in our study (Table 1). The layers of the CFs are obtained from different sources in different coordinate systems and formats (vectors, raster). Thus, each layer has been georeferenced to a common reference system (i.e., EPSG:3857 coordinate system), converted from vectors to raster, and homogenized. In order to achieve the uniformity required by ML in terms of pixel size, all layers were finally resampled to a resolution of 20 m × 20 m.

Table 2
Layers and new assigned weights for the units defined in the high-resolution CFs maps (Herrera et al., 2020).

Layer	Label	Assigned weights
Geotechnical units (Fig. 2a)	Soft cohesive soils	100
	Clays and marls with gypsum	13
	Claystones, sandstones, marls and conglomerates	6
	Alluvial-colluvial deposits	94
	Bedrock	6
Land cover (Fig. 2b)	312	1
	511	4
	333	22
	323, 324	31
	222, 242, 243, 121, 133, 112, 212, 131, 111, 223, 124, 142, 211	100
Slope (%) (Fig. 2f)	0–0.2	100
	0.2–0.5	53
	0.5–1	29
	1.01–2	25
	2.01–5	14
	5–89.74	0
Climate (Fig. 2d)	BWh	36
	BWk	12
	BSk	11

4. Methods

The overall methodological workflow employed in this study, and the generation and validation of the different LSSI maps is shown in Fig. 3. It is a cascading data flow from left to right and from top to bottom. First, a subset of the CFs originally used by Herrera et al. (2020) (geotechnical units, land cover, slope and climate) was used to generate a High-Resolution (HR) LSSI map.

Then, the set of CFs by Herrera but at higher spatial resolution and

with the addition of soft soil thickness, elevation and river distance was used, together with the HR-LSSI map, to create an enriched SD. This SD was used for training and validation sets for 22 ML models, randomly selecting 80% and 20% of the data, respectively. Specifically, the model presenting the best metrics and performance was validated with the AUC-ROC (Area Under the ROC Curve) method. Thus, the ML-LSSI map was generated by ML. Then, an FR-LSSI map was generated via the InSAR velocity map and the FR method. A comparative analysis of the three maps was finally performed using different statistical measures, namely Root Mean Square Error (RMSE), Mean Absolute Error (MAE) and Mean Absolute Percentage Error (MAPE).

4.1. Method for generating the HR-LSSI map

As explained previously, the global LSSI map generated by Herrera et al. (2020) was obtained at the spatial resolution of 1 km. Thus, the CF maps used by Herrera et al. (2020) presented a minor number of classes due to their global scale. In contrast, our study employs higher-resolution and local data presenting a higher number of classes for each CF layer. Consequently, our initial step involved reclassifying some of our detailed data using weights derived from Herrera's global-scale analysis (Herrera et al., 2020). In particular, we considered the same four CFs except for "geological units" substituted by "geotechnical units" (Fig. 2a–d and Table 2).

Subsequently, the HR-LSSI map (20 × 20 m) was calculated through the following formula, where each pixel provides an estimation of LSSI:

$$LSSI_{i,j}^{A} = \Sigma_{k=1}^{K} FR_{i,j}^{A,k}\left(f_{i,j}^{A,k}\right) \tag{1}$$

where:

$FR_{i,j}^{A,k}$ is the FR of each class (f_k) for each CF layer, and $f_{i,j}^{A,k}$ represents each class of the CFs layers.

4.2. Method for generating the ML-LSSI map

For generating the ML-LSSI map, the complete stack of the seven different CFs thematic raster was merged with a new 20 m × 20 m point grid and the HR-LSSI map. The HR-LSSI map is used as target output for the ML models, while the CFs are considered as input.

Given the heterogeneous dataset composed of several layers used in this study, the LSSI levels were not equally represented. This imbalanced distribution poses challenges for many conventional ML algorithms aimed at classification, particularly when it comes to accurately predicting the minority levels.

In our work, the task assigned to ML involves classifying LSSI levels through ML using an imbalanced dataset, aiming at accurate classification based on the six LSSI levels already used in Herrera et al. (2020). Thus, a comparative analysis of 22 ML models was performed. For further details on each classifier, the interested reader is referred for more details to text (Pedregosa et al., 2011). To further optimize the performance of the model chosen, a hyperparameter tuning was carried out, using a Bayesian optimization process (Shahriari et al., 2016; Snoek et al., 2012). Bayesian optimization is an effective strategy for tuning ML model hyperparameters, building a probabilistic model of the objective function to efficiently select new hyperparameter settings to evaluate. The probabilistic model is iteratively updated with results from new hyperparameter evaluations, to progressively achieve optimal hyperparameters (Snoek et al., 2012). Through Bayesian hyperparameter tuning, the model selected was tailored to the particular dataset and problem structure to maximize predictive accuracy. In the literature, Bayesian optimization for hyperparameter optimization is well-known for its demonstrated efficiency (Eriksson et al., 2019), as well as for its established superiority over other optimization algorithms in numerous benchmark optimization functions (Jones, 2001). In addition, Bayesian optimization has been widely employed for hyperparameter tuning of ML models applied to geological and geotechnical engineering (Li et al., 2022; Diaz and Spagnoli, 2023).

The following performance metrics have been considered to retrieve the best model and to evaluate the performance of the different ML algorithms: accuracy, precision, recall (sensitivity), specificity, F1-score, unweighted and weighted average. Let us consider, for a given set of items and for a given *i-th* class, the total number of items belonging (*P*, positive) and not belonging (*N*, negative) to that class. Let us consider a classifier, and let us denote as *TP* the true positives, i.e. the number of items correctly assigned to the class; *FP* the false positives, i.e. the number of items incorrectly assigned to the class; *FN* the false negatives, i.e. the number of items incorrectly not assigned to the class; TN the number of items correctly not assigned to the class. Then, the following measures can be defined:

$$Accuracy_i = \frac{TP + TN}{TP + FN + TN + FP} \tag{2}$$

$$Precision_i = \frac{TP}{TP + FP} \tag{3}$$

$$Recall_i \text{ or } Sensitivity_i = \frac{TP}{TP + FN} \tag{4}$$

$$Specificity_i = \frac{TN}{TN + FP} \tag{5}$$

$$F1score_i = 2 \cdot \frac{Precision \cdot Recall}{Precision + Recall} \tag{6}$$

$$Balanced\ Accuracy_i = \frac{Sensitivity_i + Specificity_i}{2} \tag{7}$$

In other words, accuracy measures the percentage of correctly classified items, while precision measures the accuracy of positive classifications (i.e., the percentage of correct positive classifications over items classified as positive). Recall, also known as sensitivity, measures the completeness of positive classifications (i.e., the percentage of correct positive classifications over the total number of actual positive items in the dataset). Specificity, or true negative rate, measures the proportion of actual negative items that are correctly classified as negative. Finally, the F1score is the harmonic mean of precision and recall, that is approximately the average of these two metrics when they are close. Balanced accuracy is a measure that averages the recall from each class (sensitivity and specificity (to provide a more comprehensive metric that accounts for imbalanced datasets by considering both the true positive rate and the true negative rate.

To combine the above per-class metrics in a global performance metric, the following measures can be defined:

$$\text{Average} = \frac{1}{C}\sum_{i=1}^{C} PM_i \tag{8}$$

$$\text{Weighted Average} = \frac{\sum_{i=1}^{C} Performancemetric_i{}' \bullet c_i}{\sum_{i=1}^{C} c_i} \tag{9}$$

where *PM* is the performance metric, *C* is the number of classes, and c_i the number of items belonging to the *i-th* class. However, the weighted average is more appropriate for dataset with unbalanced classes.

To further handle and address the challenges posed by imbalanced levels, the performance evaluation was measured using AUC-ROC for each level, using two strategies:

(i) *One-v-Rest (OvR)*, in which a binary classifier is trained for each level against the rest of the levels. The AUC-ROC score is then calculated separately for each binary classifier.

(ii) *Weighted AUC*, a *variant* of the AUC-ROC (Area Under the Curve of Receiver Operating Characteristic) metric that considers the AUC values are weighted by the level proportions: the weight of each level is proportional to its frequency (or sample size) in the dataset. This approach ensures that the evaluation metric gives the same importance to the performance of the minority or underrepresented levels.

To generate performance measures that are as independent from the dataset as possible, the cross-validation technique was employed: (i) the dataset was divided into k subsets (folds); (ii) for each fold, training was conducted on the remaining k-1 folds, while validation was performed on that specific fold; (iii) the average validation performance was computed. Specifically, we utilized the stratified k-Fold cross-validation method with k = 10. In the stratified approach, each individual fold was generated as a representative sample of the entire original dataset. This is particularly crucial for unbalanced datasets and serves as an additional measure alongside the traditional training-test split to verify its randomness.

4.3. Method for generating the FR-LSSI map

Given a study area affected by land subsidence, and several related CFs, FR can be computed as:

$$FR_{i,j}^{A,k} = \frac{subsidence\ ratio}{area\ ratio} = \left(\frac{\left(\frac{\#\ pixels\ i,j\ with\ s_{i,j}^{A}=1\ and\ class\ f_k}{\#\ pixels\ i,j\ with\ s_{i,j}^{A}=1} \right)}{\left(\frac{\#\ pixels\ i,j\ with\ class\ f_k}{\#\ pixels\ i,j\ in\ A} \right)} \right) \quad (13)$$

where:

$FR_{i,j}^{A,k}$ (f_k) is the frequency ratio of each class for each CF layer, *# pixels i,j with* $S_{i,j}^{A} = 1$ and class f_k is the number of pixels in class f_k in the land subsidence area; *# pixels i,j with* $S_{i,j}^{A} = 1$ is the total number of pixels where land subsidence occurs in the total $S_{i,j}^{A}$; *# pixels i,j with class* f_k is the number of pixels of class f_k in the whole study area and *# pixels i,j in A* is the total number of pixels in the whole study area. Finally, the different weights retrieved assigned to each pixel of all CFs are then summed together according to Formula (1).

This is a bivariate statistical model aimed at retrieving the ratio between the area where land subsidence occurs with respect to the total study area, and the ratio of the probability of land subsidence occurrence with respect to no-occurrence, for each class of all CFs.

Thus, the FR can be defined as a cross correlation between the different classes of each CF of a certain pixel and the effective land subsidence of the same pixel (Elmahdy et al., 2020). As a result, FR identifies which CFs influence the land subsidence.

The first step for LSSI mapping through FR is the creation of the SD (Herrera et al., 2020; Bianchini et al., 2019; Elmahdy et al., 2020) which consists of two parts. The first part is the land Subsidence Inventory (SI) consisting of the real detected land subsidence in a certain area. SI can be obtained using different techniques but InSAR and other geodetic techniques are the main sources of information (Herrera et al., 2020; Bianchini et al., 2019). The second part is the CFs, a set of layers of ground characteristics that might affect the LSS. Then the relationship between known subsiding areas and the CFs is calculated and the LSSI is estimated.

In this work, the SD used to generate the FR-LSSI map consists of the SI represented by the mean annual deformation velocity map measured by InSAR in the satellite Line-Of-Sight (LOS), and the same CFs used for the HR-LSSI map (Fig. 2a–d). In particular, the InSAR data are acquired by the European Space Agency (ESA) ENVISAT satellite, in descending orbit covering October 2003 to December 2008 which has been considered as a drought period in previous studies (Tomás et al., 2005), and ascending orbit covering August 2003 to July 2008. ENVISAT SAR images have been processed using SBAS-InSAR, a processing method

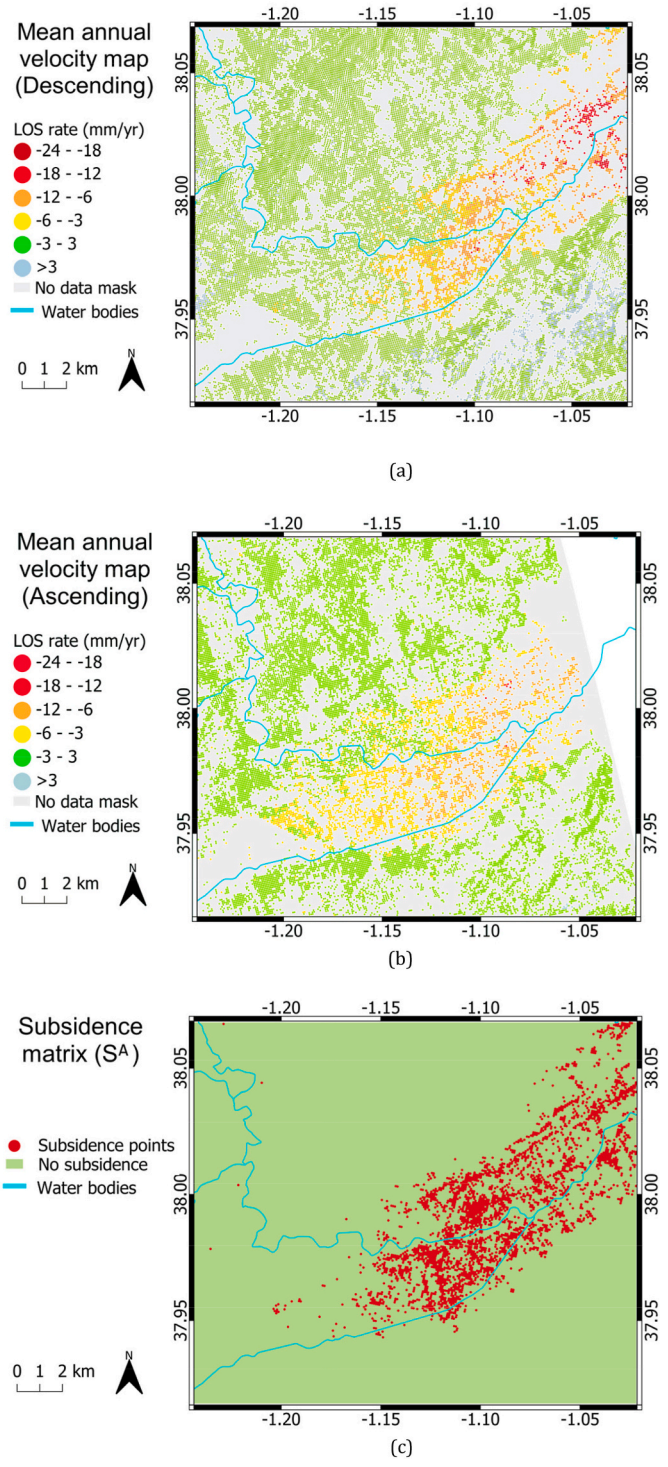

Fig. 4. InSAR derived target output: (a) total deformation map of the AOI of Murcia in the LOS projection, Descending orbit, obtained through the SBAS-InSAR technique covering the period from October 2003 to December 2008; (b) total deformation map of the AOI of Murcia in the LOS projection, Ascending orbit, covering the period from August 2003 to July 2008; c) generation of a land subsidence matrix S^A, representing in red color only pixels subject to subsidence.

based on the P-SBAS technique (Casu et al., 2014). The P-SBAS calculates the time–series of cumulative displacements and average velocity maps at a ground pixel resolution of 80 m. The average velocity pattern is 3 mm/yr of subsidence, with the rates higher in the center of the Segura valley where, the AOI values in the northeastern sector are up to

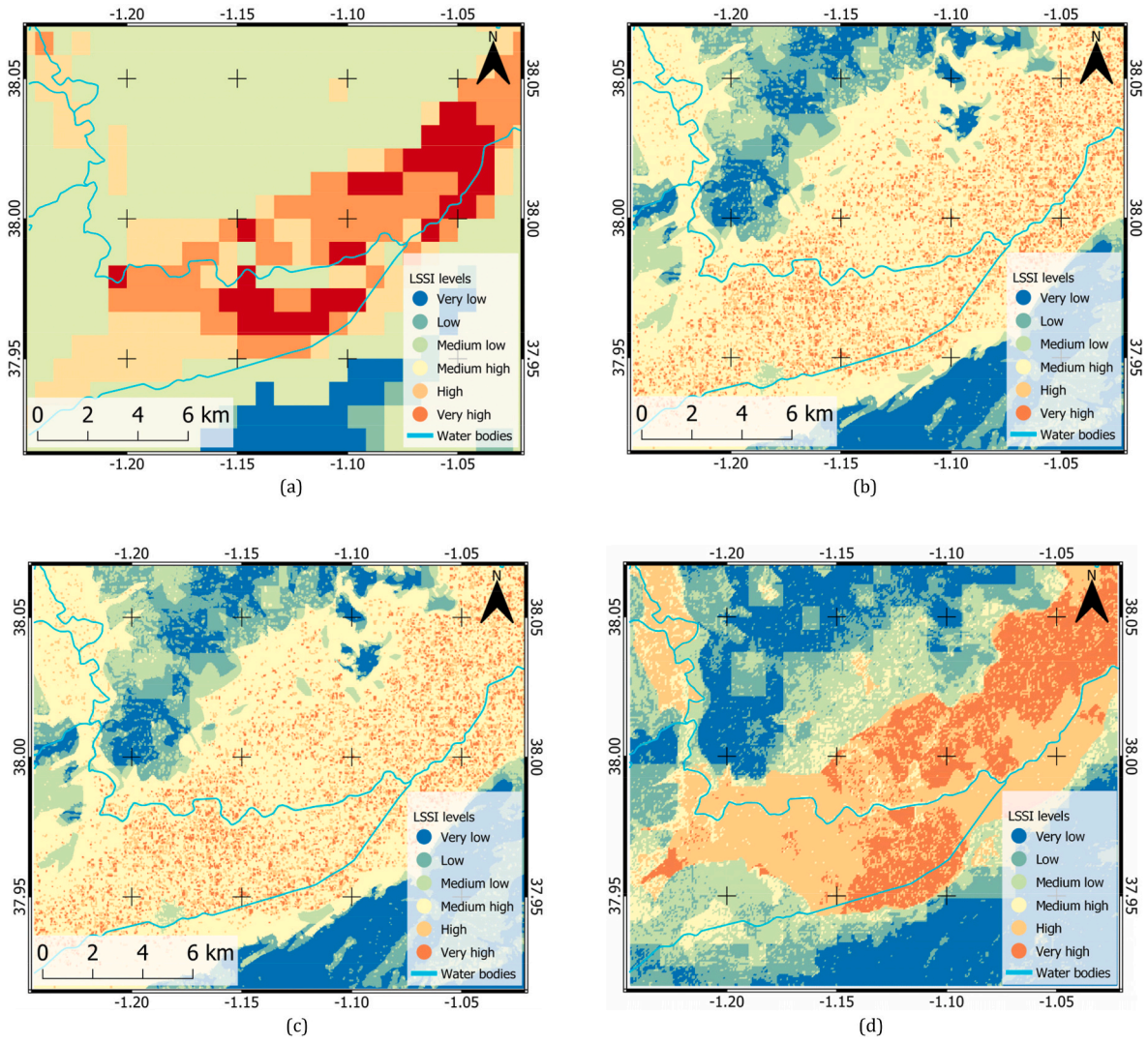

Fig. 5. Comparison between the different LSSI maps obtained: a) GSS map; b) HR-LSSI; (c) ML-LSSI and (d) FR-LSSI.

−20 mm/yr and −15 mm/yr in the descending and the ascending orbits respectively. On the contrary, areas in the northwest and southeast of the AOI remain with almost no deformation. The patterns here observed by InSAR coincide with the land subsidence trends found in other works (Tomás et al., 2005; Tessitore et al., 2016).

Fig. 4 shows the generation of the InSAR target output. Notably, the InSAR velocity maps in descending and ascending are analogous, indicating that the surface motion is consistent with vertical subsidence without any significant horizontal component. This finding aligns with other subsidence measurements in the area (Tessitore et al., 2016). However, the ascending data has lower coherence and does not cover the study area as extensively as the descending data (Fig. 4b) (Orlandi et al., 2022). Moreover, decomposing the displacement field would require focusing only on common pixels between the two orbits, which would significantly reduce the area available for analysis. Thus, for our study area, land subsidence distribution is derived from the InSAR descending data (Fig. 4a). Specifically, the InSAR land subsidence map is converted into a land subsidence matrix S^A (Fig. 4c), at a spatial resolution of 80 m. The land subsidence matrix is defined as $S^A_{i,j} \in \{1, 0\}$, where pixels have a value of 1 if land subsidence occurred (pixels showing velocity rates below −3 mm/yr, in red in Fig. 4b) and 0 if there is no record of land subsidence (pixels showing velocity rates between 0 and 3 mm/yr, in green in Fig. 4b). In particular, for the area of Murcia, there are 6395 pixels affected by land subsidence, while 76108 pixels are stable (total pixels are 82503).

Finally, the CFs (geotechnical units, land cover, slope and climate) were converted into grids at the same spatial resolution of S^A and subdivided into the classes of each CF. The FR-LSSI map (80 m × 80 m) was then generated via the FR method (Herrera et al., 2020; Arabameri et al., 2021), above explained.

4.4. Validation of the LSSI maps

In order to compare different LSSI maps, three statistical metrics have been used, namely Root Mean Square Error (RMSE), Mean Absolute Error (MAE) and Mean Absolute Percentage Error (MAPE). More formally, an LSSI map is an M × N matrix of elements $LSSI(n,m) \in \boldsymbol{LSSI}$. Given a target LSSI map and a modelled LSSI map, namely $LSSI_{TAR}$ and $LSSI_{MOD}$, the following errors were calculated to evaluate the performance of the prediction methods:

$$RMSE = \sqrt{\frac{\sum_{n,m}^{N,M}[LSSI_{MOD}(n,m) - LSSI_{TAR}(n,m)]^2}{M \times N}} \tag{11}$$

$$MAE = \frac{\sum_{n,m}^{N,M}|LSSI_{MOD}(n,m) - LSSI_{TAR}(n,m)|}{M \times N} \tag{12}$$

Table 3
Performance evaluation of machine learning models using features without and with encoding and normalization.

Model	Without encoding nor normalization			With encoding and normalization		
	Accuracy	Balanced Accuracy	F1-Score	Accuracy	Balanced Accuracy	F1-Score
Extremely Randomized Trees	**.96**	**.94**	**.96**	.96	.94	.96
RandomForestClassifier	.95	.93	.95	.95	.93	.95
BaggingClassifier	.94	.92	.94	.95	.92	.95
DecisionTreeClassifier	.94	.91	.94	.94	.91	.94
KNeighborsClassifier	.90	.85	.90	.90	.85	.90
Light Gradient Boosting Machine Classifier	.87	.82	.87	.87	.82	.87
Support Vector Classifier	.74	.59	.70	.74	.57	.72
GaussianNB	.45	.54	.48	.45	.54	.48
NearestCentroid	.46	.52	.49	.46	.52	.49
Bernoulli Naive Bayes	.57	.46	.55	.57	.57	.59
LinearDiscriminantAnalysis	.66	.44	.59	.66	.56	.65
QuadraticDiscriminantAnalysis	.56	.38	.56	.56	.38	.56
PassiveAggressiveClassifier	.63	.38	.56	.60	.32	.57
LogisticRegression	.67	.38	.60	.67	.45	.62
CalibratedClassifierCV	.67	.37	.59	.68	.45	.64
LinearSVC	.67	.35	.57	.68	.43	.61
Perceptron	.57	.35	.53	.60	.37	.58
AdaBoostClassifier	.61	.31	.51	.61	.31	.51
RidgeClassifier	.65	.31	.55	.68	.41	.60
RidgeClassifierCV	.65	.31	.55	.68	.41	.60
Stochastic Gradient Descent Classifier	.64	.3	.56	.67	.42	.63
DummyClassifier	.57	.17	.41	.57	.17	.41

$$MAPE = \frac{100}{M \times N} \cdot \frac{\sum_{n,m}^{N,M} |LSSI_{MOD}(n,m) - LSSI_{TAR}(n,m)|}{LSSI_{TAR}(n,m)} \quad (13)$$

Table 4
Optimal hyperparameters of the ERT model, achieved via Bayesian optimization.

Hyperparameter	Optimal Value	Description
n-estimators	1820	The number of trees in the forest
criterion	'gini'	A measure of the quality of the split.
max_depth	None	The max. depth of the tree. None means all nodes are expanded.
min_samples_split	2	The min. number of samples required to split an internal node
min_samples_leaf	1	The minimum number of samples required to be at a leaf node.
min_weight_fration_leaf	0.0	The minimum weighted fraction of the sum total of weights (of all the input samples) required to be at a leaf node.
max_features	None	The number of features to consider when looking for the best split.
max_leaf_nodes	None	Best nodes are defined as relative reduction in impurity.
min_impurity_decrease	0.0	A node will be split if this split induces a decrease of the impurity greater than or equal to this value.
bootstrap	False	Whether bootstrap samples are used when building trees. If False, the whole dataset is used to build each tree.
oob_score	False	Whether to use out-of-bag samples to estimate the generalization score. Only available if bootstrap = True.
n_jobs	None	The number of jobs to run in parallel.
random_state	None	It controls the source of randomness.
verbose	0	Controls the verbosity when fitting and predicting.
warm_start	False	It is used to fit a whole new forest.
class_weight	balanced	Weights associated with classes in the form.
ccp_alpha	0.0	Complexity parameter used for Minimal Cost-Complexity Pruning.
max_samples	None	The number of samples to draw.

5. Results and discussion

5.1. LSSI mapping

In this study, LSS phenomenon was explored and calculated using several CFs through different approaches described in Sections 2-3. Fig. 5 shows the GSS map (Herrera et al., 2020) with a focus over the AOI (Fig. 5a) and the three LSSI maps generated, HR-LSSI (20 × 20 m), ML-LSSI (20 m × 20 m), and FR-LSSI (80 × 80 m), respectively. Overall, the maps exhibit a consistent visual pattern, with the central region of the study area displaying elevated LSS levels in all the four maps.

Results show good alignment between HR-LSSI and ML-LSSI across identical CFs, with the role of the additional CFs in ML-LSSI consistent with previous studies (Orlandi et al., 2022). First of all, a comparative analysis with Fig. 2 shows that HR-LSSI exhibits high LSSI predominantly within "soft cohesive soils", with additional susceptibility observed in the "alluvial-colluvial deposits". This pattern is closely associated with land cover classes "222" (orchards) and "242" (mosaic of crops). Climate conditions of BWh (hot deserts) dominate the region, with a minor presence of BWk (cold desert) in the northwest. Moreover, it is evident that the most of the LSS is associated with slope values ranging from 0° to 2°. Similarly, the ML-LSSI map shows high LSSI values within geotechnical units such as "soft cohesive soils" and "alluvial-colluvial deposits" and the same values of slope. The same land cover classes shared with HR-LSSI map contribute to higher susceptibility. However, the prevailing climate is BWh, with a slight influence of BWk in the northwest sector of the study area. In the ML-LSSI the impact of three other CFs can be appreciated. Starting from the elevation, most of the LSS appear to occur at elevations ranging from 25 up to 110 m a.s.l. Subsequently, the observed pattern of "soft soil thickness" aligning with areas of high LSSI suggests that these soil types are indeed more susceptible to land subsidence (Comunidad Autónoma de la Región de Murcia, 2023). Lastly, the information of the distance to the main river of Segura is particularly noteworthy, as it highlighted the importance of proximity to a water body for having higher values of LSS. In fact, most land subsidence occurs within a maximum distance of 130 m from the river, suggesting a correlation between river proximity and land subsidence as found in other previous works (Tomas et al., 2011). This is because the proximity can be linked to the presence of soft cohesive soils, which are commonly found in areas near water bodies. Other factors can include the higher density of pumping wells close to the river

Table 5
Confusion matrix achieved after the hyperparameter optimization of the ERT model.

		ML-LSSI					
		1	2	3	4	5	6
HR-LSSI	1	***7272***	68	138	7	0	0
	2	49	***3863***	176	0	0	0
	3	129	181	***94329***	928	242	136
	4	1	0	1047	***23912***	654	332
	5	0	0	227	662	***20253***	816
	6	0	0	176	189	826	***12544***

Table 6
Summary of performance metrics achieved on the test set for ML-LSSI based on ETC.

Levels	Precision	Recall	F1-Score	Support
Very Low (1)	0.98	0.97	0.97	7485
Low (2)	0.94	0.94	0.94	4088
Medium Low (3)	0.98	0.98	0.98	95945
Medium High (4)	0.93	0.92	0.92	25946
High (5)	0.92	0.92	0.92	21958
Very High (6)	0.91	0.91	0.91	13835
Average	0.94	0.94	0.94	169257
Weighted Average	0.96	0.96	0.96	169257

and the groundwater dynamics. On the other hand, despite its lower resolution, FR-LSSI exhibits defined LSSI patterns, with some differences in the dominating geotechnical and land cover units. For instance, FR-LSSI identifies susceptibility primarily within geotechnical units characterized by "soft cohesive soils" in the northwest and central parts of the AOI. This pattern of geotechnical-related LSS can also be found in previous studies (Tomas et al., 2011). The land cover classes associated with high LSSI include "111" (continuous urban fabric), "112" (discontinuous urban fabric), "222" (orchards) and "242" (mosaic of crops), indicating a diverse range of land uses contributing to land subsidence susceptibility. Finally, similarly to the ML-LSSI map, the prevailing climate is BWh, with a presence in BWk in the northeast.

5.2. Model validation and comparison

The results of the performance of the different algorithms are summarized in Table 3. Overall, the Extremely Randomized Trees (ERT) emerged as the best model, demonstrating a robust performance with accuracy, balanced accuracy and F1-scores equal to 0.96, 0.94 and 0.96, respectively.

The process was both carried out without and with pre-processing, i.e., normalizing and encoding the variables. However, the top performing models, i.e., ERT, Random Forest Classifier, Bagging Classifier, and Decision Tree Classifier, achieved about the same performance regardless of pre-processing. Pre-processing only provided small improvements for weaker models, like Bernoulli NB and Logistic Regression. But the top models still outperformed without preprocessing due to flexible ensemble and decision tree bases. Their consistency implies an inherent capability to handle diverse raw features effectively on this particular dataset and task.

More specifically, the ERT is an ensemble tree-based ML algorithm, introduced by Geurts et al. (2006) (Geurts et al., 2006), that builds on the Random Forest algorithm by taking further steps to randomize the trees. In Random Forest, each tree is trained on a bootstrap sample of the training data, whereas ERT goes further by sampling features randomly for each node, without replacement to split on.

Tables 4 and 5 show the optimal value of each hyperparameter and the confusion matrix, respectively, for the optimized ERT model, with 80/20 train/test split.

Table 7
OvR ROC AUC values of each class and mean weighted ROC AUC score.

Metric	Average	Level 1	Level 2	Level 3	Level 4	Level 5	Level 6
OvR AUC-ROC	0.998	0.999	0.999	0.998	0.996	0.996	0.997
Weighted AUC-ROC	0.997						

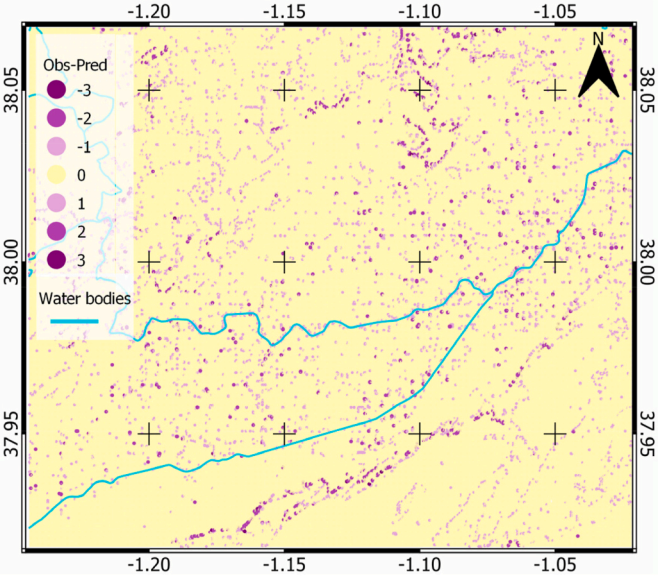

Fig. 6. Map showing the accuracy of the model pixel by pixel between the HR-LSSI map with ML-LSSI map.in yellow areas where the model predicts correctly and in scales of purple the levels of failure of prediction.

More specifically, Table 6 summarizes the performance metrics achieved on the test set for each level by ML-LSSI based on Extra-Trees Classifier (ETC).

The ETC model effectively distinguished between different classes and maintained strong metrics even for minority classes. Specifically for the minority level (1) the ETC model achieved high specificity (0.998) and sensitivity (0.971). Performance remains strong for level 2 as well, with precision 0.939, recall 0.944 and F1-score 0.942. As expected, the prevalent level 3 is handled exceptionally well, with excellent precision (0.981), recall (0.983) and F1-score (0.982), due to benefiting from substantial training data. For the smaller levels 4, 5, and 6, metrics naturally decline but are still respectable, reflecting the inherent challenge in balancing sensitivity and specificity with diminishing samples. In summary, the classifier exhibits robust performance on an imbalanced multilevel problem, maintaining strong metrics even for the smaller levels. Its flexibility and generalization capability allow effective balancing of precision and recall across all levels despite data scarcity. The classifier's resilience enables both sensitive identification of rare cases and accurate classification of common cases.

Table 7 shows the results of OvR AUC-ROC and Weighted AUC-ROC in the proposed ETC. The results indicated high performance across all levels, with OvR AUC-ROC averaging at 0.998 and consistently strong values across individual levels. The Weighted AUC-ROC also demonstrated strong performance at 0.997. These findings suggest robust discriminative ability and class separation across the different levels.

Additionally, another check was performed, and the dataset underwent Stratified k-Fold cross-validation with $k = 10$. This approach eliminates partitioning bias and offers an unbiased estimate of average performance. The results showed a mean accuracy of 0.960 and a

Table 8
Comparative analysis between ML-LSSI and the other maps, using RMSE, MAE and MAPE measures.

LSSI map	RMSE	MAE	MAPE (%)
ML-LSSI vs HR-LSSI	0.109	0.009	0.36
ML-LSSI vs FR-LSSI	1.260	0.967	42.20

balanced accuracy of 0.944 aligning closely with the original results (train test split), showing that the original validation metrics accurately reflect the true capabilities of the model. Crucially, the robust k-fold metrics, despite completely distinct data splitting on each fold, confirm that the classifier does not simply memorize the training data but can successfully generalize predictions.

However, discrepancies were noted between HR- and ML-LSSI maps.

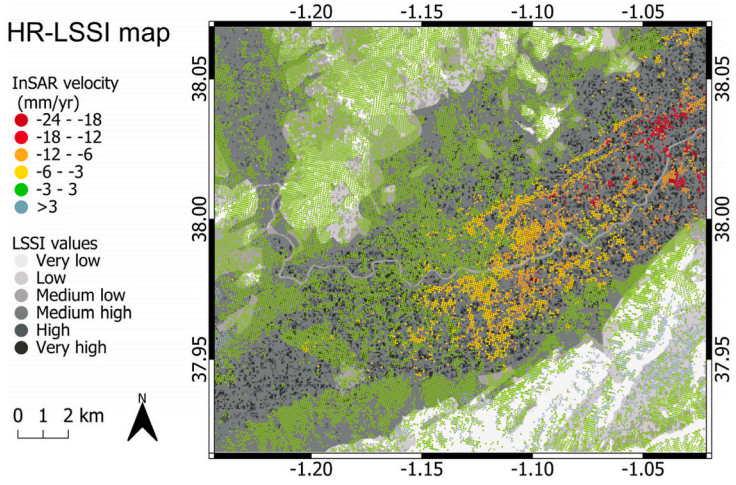

(a)

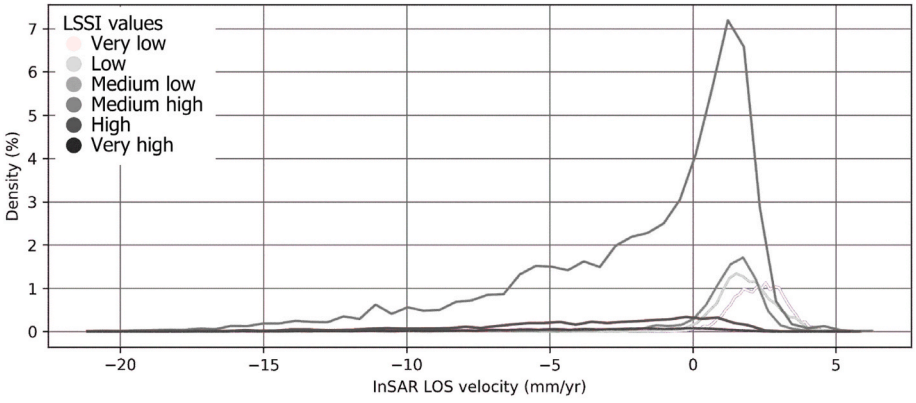

(b)

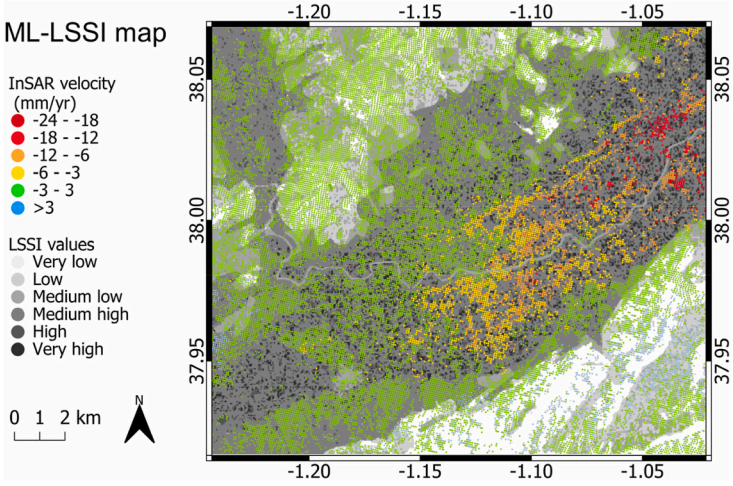

(c)

Fig. 7. Distribution of the InSAR velocity values across all the 6 LSSI classes for: a) and b) HR-LSSI map; c) and d) ML-LSSI map and e) and f) FR-LSSI map, where negative LOS values represent land subsidence.

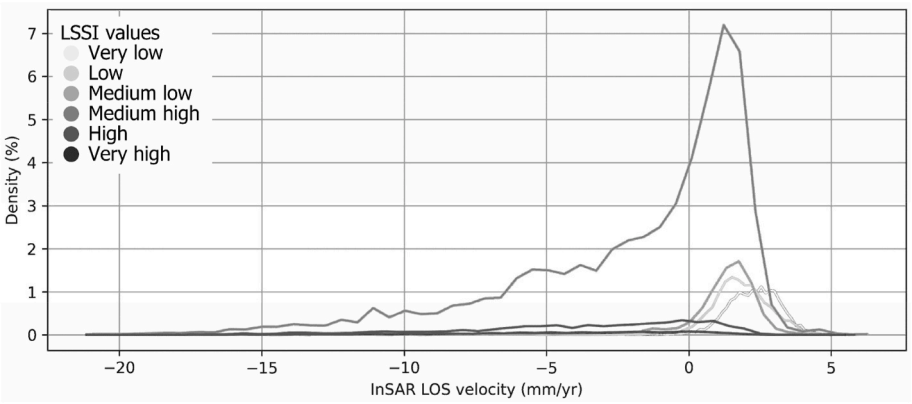

(d)

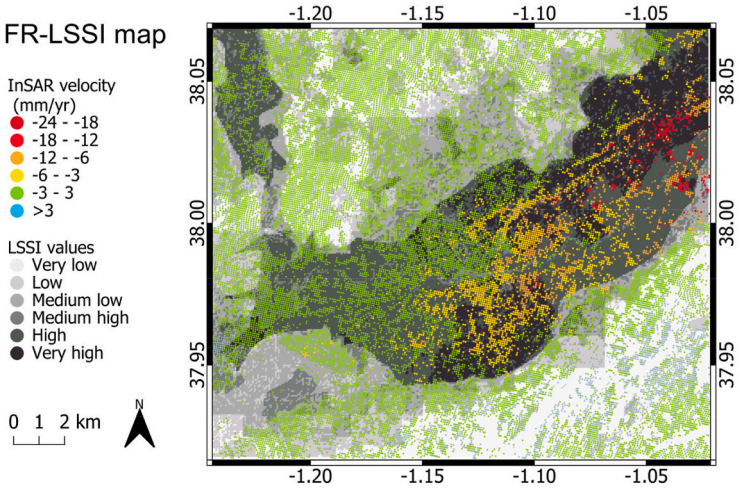

(e)

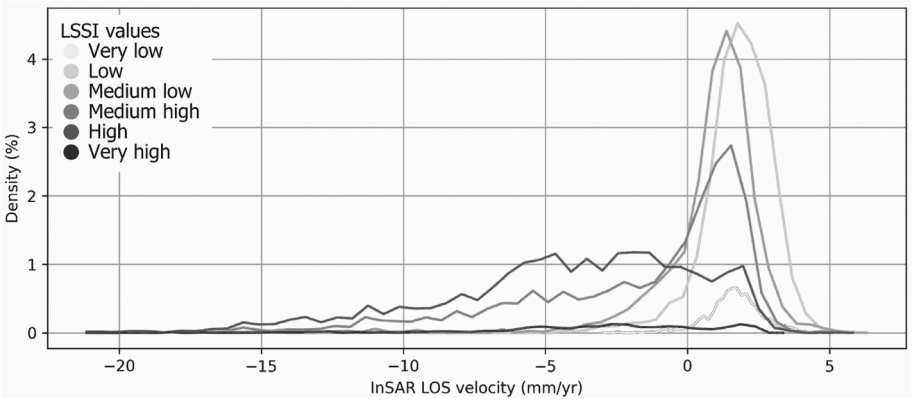

(f)

Fig. 7. (*continued*).

By comparing LSSI values between HR-(Observed) and ML-LSSI (Predicted) maps, thus representing and examining the error distribution in each LSSI class, it can be observed that the maximum error values (no more than 0.8 %, Fig. 6) coincide with certain values of elevation and geotechnical and land cover units. For instance, most of the error coincides with the boundary of the Vega Media, which in turn corresponds to the contact between "bedrock" and "alluvial-colluvial deposits" geotechnical units, which further aligns with the edge between the land cover classes of "coniferous forests" and "orchards". These discrepancies could be attributed to the introduction of additional CFs such as topographic variations, which may lead to complex interactions along valley edges and consequent inaccuracies, and environmental factors, where interactions between vegetation and different types of soil along valley edges may not be fully captured. These findings emphasize the need to

consider multiple factors and spatial resolutions when modeling LSS.

Table 8 shows a comparative analysis between ML-LSSI and the other maps, i.e., HR-LSSI and FR-LSSI. Here, the impact of spatial resolution on model performance. The ML-LSSI vs. FR-LSSI is characterized by a greater error than ML-LSSI vs. HR-LSSI, as ML-LSSI and FR-LSSI have different spatial resolution (20 m and 80 m, respectively) while ML-LSSI and HR-LSSI have the same resolution (20 m).

Finally, all the three LSSI maps have been compared to the InSAR LOS average velocity maps (Fig. 7). By analyzing the distribution of the InSAR velocity values within the six different classes of LSSI across all the three LSSI maps, we observed a significant agreement between low LSSI classes and stable LOS values. However, different findings can be drawn. Concerning the HR-LSSI and ML-LSSI maps, while areas with high LSSI values ("Medium high" class) often correspond to significant InSAR velocity ranges (up to 20 mm/yr), a notable portion of the area affected by land subsidence shows almost stable LOS values. This indicates that high susceptibility does not always coincide with land subsidence, highlighting the complexity of subsidence processes. This result is not contradictory with the concept of LSS: in fact, LSSI values may not experience subsidence, yet the area remains susceptible to land subsidence. It is worth noting that a susceptibility map highlights areas most likely to experience subsidence events. However, high susceptibility to land subsidence does not guarantee subsidence happens. For example, if triggers such as falling piezometric levels never occur then subsidence does not occur. This is likely the main reason for the discrepancies between real displacements derived from InSAR and the susceptibility maps. Conversely, greater consistency is observed in the FR-LSSI map, where the "High" susceptibility classes correspond to larger land subsidence values.

These findings underscore the importance of considering multiple factors and spatial resolutions, and also the importance of accurately assessing model performance when interpreting and validating LSS models to inform land management decisions and risk mitigation strategies.

6. Conclusions

In conclusion, our study highlights the advantages of integrating machine learning techniques with traditional methods for Land Subsidence Susceptibility mapping. The study compared multiple Land Subsidence Susceptibility maps, on the pilot area of Murcia, generated using both conventional Frequency Ratio methods and advanced Machine Learning models. More than twenty Machine Learning models were compared, over different performance metrics. The superior performance of the Extra-Trees Classifier model, suitable for analyzing vast geospatial datasets and to outperform traditional methods, demonstrates the potential for these approaches to enhance land subsidence susceptibility assessment. Specifically, the Land Subsidence Susceptibility maps were validated using InSAR satellite data, confirming the reliability and accuracy of the Machine Learning generated maps. This validation underscores the importance of high spatial resolution in improving land subsidence susceptibility assessments. The analysis carried out in the area of Murcia revealed that while incorporating multiple Conditioning Factors is beneficial, their effectiveness is highly dependent on the characteristics of each data layer. This finding emphasizes the need for careful selection and optimization of Conditioning Factors in Land Subsidence Susceptibility mapping. Future research should focus on further refining these models and exploring the integration of additional high-resolution datasets to improve the accuracy and reliability of land subsidence susceptibility maps."

CRediT authorship contribution statement

Diana Orlandi: Writing – review & editing, Writing – original draft, Software, Methodology, Investigation, Data curation, Conceptualization. **Esteban Díaz:** Writing – review & editing, Writing – original draft, Software, Project administration, Methodology, Investigation, Funding acquisition, Data curation, Conceptualization. **Roberto Tomás:** Writing – review & editing, Writing – original draft, Project administration, Methodology, Investigation, Funding acquisition, Data curation, Conceptualization. **Federico A. Galatolo:** Writing – review & editing, Writing – original draft, Software, Methodology, Investigation. **Mario G. C.A. Cimino:** Writing – review & editing, Writing – original draft, Project administration, Methodology, Investigation, Funding acquisition. **Carolina Pagli:** Writing – review & editing, Writing – original draft, Methodology, Investigation. **Nicola Perilli:** Writing – review & editing, Methodology, Investigation.

Ethics approval and consent to participate

Not applicable.

Consent for publication

Not applicable.

Declaration of competing interest

The authors declare that they have no known competing financial interests or personal relationships that could have appeared to influence the work reported in this paper.

Acknowledgments

This research is supported by the Ministry of University and Research (MUR) as part of the PON 2014–2020 "Research and Innovation" resources – Green/Innovation Action – DM MUR 1061/2022. Work partially supported by: (i) the University of Pisa, in the framework of the PRA 2022 101 project "Decision Support Systems for territorial networks for managing ecosystem services"; (ii) the European Commission under the NextGenerationEU program, Partenariato Esteso PNRR PE1 - "FAIR - Future Artificial Intelligence Research" - Spoke 1 "Human-centered AI"; (iii) the Italian Ministry of Education and Research (MIUR) in the framework of the FoReLab project (Departments of Excellence). Partially financed by the European Union—NextGenerationEU (National Sustainable Mobility Center CN00000023, Italian Ministry of University and Research Decree n. 1033—17/06/2022, Spoke 10). Roberto Tomás and Esteban Díaz are also supported by the Conselleria de Innovación, Universidades, Ciencia y Sociedad Digital in the framework of the project CIAICO/2021/335, the ESA-MOST China DRAGON-5 project with ref. 59339 and DRAGON-6 project with ref. 95355, the EU project "Sustainable groundwater resources management by integrating earth observation derived monitoring and flow modeling results (RESERVOIR)" Grant agreement No. 1924 and the programme Marie Skłodowska-Curie Actions - Staff Exchange (SE) Grant agreement No. 101131146. CP acknowledges the Space It Up project funded by the Italian Space Agency, ASI, and the Ministry of University and Research, MUR, under contract n. 2024-5-E.0 - CUP n. I53D24000060005.

Appendix A. Supplementary data

Supplementary data to this article can be found online at https://doi.org/10.1016/j.acags.2024.100207.

Data availability

Data will be made available on request.

References

Arabameri, A., Yariyan, P., Santosh, M., 2021. Land subsidence spatial modeling and assessment of the contribution of geo-environmental factors to land subsidence:

comparison of different novel ensemble modeling approaches. PREPRINT Version 1. https://doi.org/10.21203/rs.3.rs-194202/v1. Research Square.
Bagheri-Gavkosh, M., Hosseini, S.M., Ataie-Ashtiani, B., Sohani, Y., Ebrahimian, H., Morovat, F., Ashrafi, S., 2021. Land subsidence: a global challenge. Sci. Total Environ. 778, 146193. https://doi.org/10.1016/j.scitotenv.2021.146193.
Beck, H.E., Zimmermann, N.E., McVicar, T.R., Vergopolan, N., Berg, A., Wood, E.F., 2018. Present and future Köppen-Geiger climate classification maps at 1-km resolution. Sci. Data 5, 180214. https://doi.org/10.1038/sdata.2018.214.
Bianchini, S., Solari, L., Del Soldato, M., Raspini, F., Montalti, R., Ciampalini, A., Casagli, N., 2019. Ground subsidence susceptibility (GSS) mapping in Grosseto Plain (tuscany, Italy) based on satellite InSAR data using frequency ratio and Fuzzy logic. Rem. Sens. 11 (17), 2015.
Casu, F., Elefante, S., Imperatore, P., Zinno, I., Manunta, M., De Luca, C., Lanari, R., 2014. SBAS-DInSAR parallel processing for deformation time-series computation. IEEE JSTARS. https://doi.org/10.1109/JSTARS.2014.2322671.
Cigna, F., Tapete, D., 2021. Present-day land subsidence rates, surface faulting hazard and risk in Mexico City with 2014-2020 Sentinel-1 IW InSAR. Rem. Sens. Environ. 253, 112161.
Cimino, M.G., Ennahedh, M., Galatolo, F.A., Hariga-Tlatli, N., Nouiri, I., Perilli, N., Tarhouni, J., 2022. A machine learning approach for groundwater modeling. In: 2022 IEEE 9th International Conference on Sciences of Electronics, Technologies of Information and Telecommunications (SETIT), pp. 299–304. IEEE.
Comunidad Autónoma de la Región de Murcia, 2023. Informe sobre la "Consejería de Obras Públicas, Vivienda y Transportes" [descarga (carm.es)]. (2023).
Confederación Hidrográfica del Segura, O.A., 2023. Descarga de cartografía en formato SHP, 2023. https://www.chsegura.es/es/cuenca/cartografia/descarga-de-cartografia-en-formato-shp/.
Diaz, E., Spagnoli, G., 2023. Gradient boosting trees with bayesian optimization to predict activity from other geotechnical parameters. Mar. Georesour. Geotechnol. https://doi.org/10.1080/1064119X.2023.2251025.
Elmahdy, S.I., Mohamed, M.M., Ali, T.A., Abdalla, J.E.D., Abouleish, M., 2020. Land subsidence and sinkholes susceptibility mapping and analysis using random forest and frequency ratio models in Al Ain, UAE. Geocarto Int. 37 (1), 315–331. https://doi.org/10.1080/10106049.2020.1716398.
Eriksson, D., Pearce, M., Gardner, J., Turner, R.D., Poloczek, M., 2019. Scalable global optimization via local bayesian optimization. Adv. Neural Inf. Process. Syst. 32.
European Environment Agency (EEA), 2006. CORINE Land Cover 2006. Retrieved from [CORINE Land Cover 2006 (vector/raster 100 m), Europe, 6-yearly — Copernicus Land Monitoring Service].
Fabris, M., Battaglia, M., Chen, X., Menin, A., Monego, M., Floris, M., 2022. An integrated InSAR and GNSS approach to monitor land subsidence in the Po river delta (Italy). Rem. Sens. 14 (21), 5578.
Galloway, D.L., Burbey, T.J., 2011. Review: regional land subsidence accompanying groundwater extraction. Hydrogeol. J. 19, 1459–1486.
Geurts, P., Ernst, D., Wehenkel, L., 2006. Extremely randomized trees. Mach. Learn. 63 (1), 3–42.
Herrera, G., Tomás, R., Monells, D., Centolanza, G., Mallorquí, J.J., Vicente, F., Navarro, V.D., Lopez-Sanchez, J.M., Sanabria, M., Cano, M., Mulas, J., 2010. Analysis of subsidence using TerraSAR-X data: Murcia case study. Eng. Geol. 116, 284–295.
Herrera, G., Ezquerro, P., Tomás, R., Bejar, M., Vinielles, J., Rossi, M., Mateos, R., Carreon, D., Lamber, J., Teatini, P., Cabral-Cano, E., Erkens, G., Galloway, D., Hung, W.-C., Kakar, N., Sneed, M., Tosi, L., Wan, H., Ye, S., 2020. Mapping the global threat of land subsidence. Science 371 (6524), 34–36. https://doi.org/10.1126/science.abb0340.
Hu, L., Navarro-Hernández, M.I., Liu, X., Tomás, R., Tang, X., Bru, G., Ezquerro, P., Zhang, Q., 2022. Analysis of regional large-gradient land subsidence in the Alto Guadalentín Basin (Spain) using open-access aerial LiDAR datasets. Rem. Sens. Environ. 280, 113218.
IGME, 2000. Estudio geotécnico del subsuelo del área metropolitana de Murcia. Instituto geológico y Minero de España y Consejería de Obras Públicas y Ordenación territorial de la Región de Murcia. Internal report, p. 120.
Jones, D.R., 2001. A taxonomy of global optimization methods based on response surfaces. J. Global Optim. 21, 345–383.
Li, D., Liu, Z., Xiao, P., Zhou, J., Jahed Armaghani, D., 2022. Intelligent rockburst prediction model with sample category balance using feedforward neural network and Bayesian optimization. Undergr. Space 7, 833–846. https://doi.org/10.1016/j.undsp.2021.12.009.
Loupasakis, C., Tzampoglou, P., 2017. Land Subsidence Susceptibility and Hazard Mapping: the Case of Amyntaio Basin, Greece. https://doi.org/10.1117/12.2277510.
Organismo Autónomo Centro Nacional de Información Geográfica (CNIG), 2023. Modelo Digital del Terreno - MDT05, 2023. https://centrodedescargas.cnig.es/CentroDescargas/.
Orlandi, D., Galatolo, F.A., Cimino, M.G., La Rosa, A., Pagli, C., Perilli, N., 2022. Enhancing Land Subsidence Awareness via InSAR Data and Deep Transformers. IEEE Conference on Cognitive and Computational Aspects of Situation Management (CogSIMA), IEEE, pp. 98–103, 2022, June.
Pedregosa, F., et al., 2011. Scikit-learn: machine learning in Python. J. Mach. Learn. Res. 12, 2825–2830.
Pradhan, B., Abokharima, M., Jebur, M., Tehrany, M., 2014. Land subsidence susceptibility mapping at Kinta Valley (Malaysia) using the evidential belief function model in GIS. Nat. Hazards 73. https://doi.org/10.1007/s11069-014-1128-1.
Rahmati, O., Golkarian, A., Biggs, T., Keesstra, S., Mohammadi, F., Daliakopoulos, I.N., 2019. Land subsidence hazard modeling: machine learning to identify predictors and the role of human activities. J. Environ. Manag. 236, 466–480. https://doi.org/10.1016/j.jenvman.2019.02.020.
Rezaei, M., Noori, Z., Dashti, B.M., 2020. Land subsidence susceptibility mapping using analytical Hierarchy process (AHP) and certain factor (CF) models at Neyshabur plain, Iran. Geocarto Int. 37, 1–20.
Saha, A., Villuri, V.G.K., Bhardwaj, A., 2023. Development and assessment of a novel hybrid machine learning-based landslide susceptibility mapping model in the Darjeeling Himalayas. Stoch. Environ. Res. Risk Assess. 1–24.
Shahriari, B., Swersky, K., Wang, Z., Adams, R.P., de Freitas, N., 2016. Taking the human out of the loop: a review of Bayesian optimization. Proc. IEEE 104 (1), 148–175.
Snoek, J., Larochelle, H., Adams, R.P., 2012. Practical Bayesian optimization of machine learning algorithms. In: Advances in Neural Information Processing Systems, pp. 2951–2959.
Tessitore, S., Fernandez-Merodo, J.A., Herrera, G., Tomás, R., Ramondini, M., Sanabria, M., Duro, J., Mulas, J., Calcaterra, D., 2016. Comparison of water-level, extensometric, DInSAR and simulation data for quantification of subsidence in Murcia City (SE Spain). Hydrogeol. J. 24. https://doi.org/10.1007/s10040-015-1349-8.
Tien Bui, D., Shahabi, H., Shirzadi, A., Chapi, K., Pradhan, B., Chen, W., Khosravi, K., Panahi, M., Bin Ahmad, B., Saro, L., 2018. Land subsidence susceptibility mapping in South Korea using machine learning algorithms. Sensors 18, 2464. https://doi.org/10.3390/s18082464.
Tomás, R., Márquez, Y., Lopez-Sanchez, J.M., Delgado, J., Blanco, P., Mallorquí, Martínez, M., Herrera, G., Mulas, J., 2005. Mapping ground subsidence induced by aquifer overexploitation using advanced Differential SAR Interferometry: Vega Media of the Segura River (SE Spain) case study. Rem. Sens. Environ. 98 (2–3), 269–283.
Tomas, R., Herrera, G., Cooksley, G., Mulas, J., 2011. Persistent Scatterer Interferometry subsidence data exploitation using spatial tools: the Vega Media of the Segura River Basin case study. J. Hydrol. 400, 411–428. https://doi.org/10.1016/j.jhydrol.2011.01.057.
Wang, H., Gong, H., Chen, B., Zhou, C., Yang, Y., Sun, X., 2024. Research on land subsidence-rebound affected by dualistic water cycle driven by climate change and human activities in Dezhou City, China. J. Hydrol. 636, 131327.